Supporting information

Piezoelectric Nanogenerators with Hybrid Nanofibers: A Dual Approach for Energy Generation and Wastewater Treatment

Manish Kumar[1], Sumit Choudhary[2,3], Satinder K. Sharma[2] and Jaspreet Kaur Randhawa[1]*
[1]School of Mechanical and Material Engineering, Indian Institute of Technology Mandi, India
[2]Department of Engineering & Technology, Gurugram University
[3]School of Computing and Electrical Engineering, Indian Institute of Technology Mandi, India

*Corresponding author: jaspreet@iitmandi.ac.in

*Corresponding Author's Address
Dr. Jaspreet Kaur Randhawa
Associate Professor
School of Engineering,
Indian Institute of Technology Mandi, India

Table of content

Figure S5: X-Ray Diffraction (XRD) spectra comparison between (a) PAN NFs, (b) Electrospun α- Fe2O3/PAN, (MNFs) mat and (c) Electrospun calcined MNF-C.

Figure S6: Fourier Transform Infrared Spectroscopy (FTIR) spectra of (a) MNFs and (b) MNFs-C.

Table S2 FTIR analysis of MNFs and MNFs-C

Figure S7: (a) Contact angle measurement and (b) Thermogravimetric Analysis (TGA) and DSC analysis of (b) MNFs-C. and (b) MNFs.

Figure S8: The voltage and current of the piezo device on the application of tapping force Stability of the PENG device

Figure S9: Schematic of photocatalytic degradation mechanism of MB

Table S3: A comprehensive representation of photocatalytic degradation of organic dyes as reported in literature.

Figure S 10: Sonocatalytic performance comparison among (a) With MB without any catalyst (b) with PAN nanofiber, (c) with MNFs, and (d) degradation percentage, (e)Mechanism of sonocatalytic.

Table S4: Comparison Table of Sonocatalysis of Various Organic Dyes in the Literature

Figure S11: Pyro catalytic performance comparison among (a) With MB without any catalyst, (b) with PAN nanofiber, (c) with MNFs, and (d) degradation percentage, (e) mechanism of pyro catalytic.

Table S5: Comparative study of Pyro catalytic activity of MNFs with some reported catalysts in the degradation of various dyes.

Figure S12: Depiction of intermediate species formed in the process of photocatalytic degradation studies following two pathways: (a) Sequential degradation of MB and (b) Immediate degradation of MB respectively.

Figure S13: Mass Spectrometry analysis of the intermediates of MB.

Figure S14: (a) MB removal using MNFs mat with 10 ppm and 20 ppm concentrations. (b) MB filtration using MNFs NFs for higher concentrations (50-200 ppm). Inset of Figure 3b shows MB percentage removal efficiency at various concentrations (10-200 ppm).

Figure S15: Illustration of adsorption and desorption of MB dye.

Figure S16. XPS spectra of the MNFs NFs. (a) Full survey XPS spectrum (b) High resolution C1s spectra (c) High resolution N1s spectra (d) Deconvoluted high Fe2p spectra and (e) High resolution O1s spectra respectively.

Figure S17. XPS spectra of the MNFs NFs after MB absorption. (a) Full survey XPS spectrum (b) High resolution C1s spectra (c) High resolution N1s spectra (d) Deconvoluted high Fe2p spectra and (e) High resolution O1s spectra and (f) HOMO LUMO energy band gap for MNFs nanofibers respectively.

Figure S18: (a) Lead adsorption pseudo second order kinetic model, (b) removal efficiency of lead, (c) copper adsorption pseudo second order kinetic model, and (d) removal efficiency of copper respectively.

Table S6: Elemental study comparison of MNFs mat before and after heavy metals adsorption.

Figure S19: SEM images and Energy Dispersive X-ray Analysis (EDAX) of MNFs mat after heavy metal filtration. (a, b) SEM and EDAX spectra after Pb filter, (c, d) SEM and EDAX spectra after Cu filter.

1. Experimental

1.1 Materials and method

The following materials were obtained from Sigma Aldrich: polyacrylonitrile (PAN) polymer with a molecular weight of 150 KDa, dimethylformamide (DMF), ethanol, iron (III) nitrate, atomic absorption standard solutions for lead and copper with a concentration of 1000ppm, methylene blue, and Whatman filter paper. These materials were utilized as received without any additional purification. The current investigation was conducted using deionized water with a resistivity of 18.2MΩ/cm.

1 Material characterization

Nanofiber fabrication was performed using the E-spin Nanotech Super ES-2 electrospinning model. Surface morphology analysis of the MNFs mat was conducted using a FESEM (NOVA Nano SEM 450) with a 10 kV acceleration voltage, and FESEM-EDAX was performed to analyse elemental composition. Brunauer-Emmett-Teller (BET) surface area and pore volume studies were carried out using a Quanta chrome Autosorb IQ-3 nitrogen analyser to evaluate adsorption-desorption isotherm and surface area. TEM analysis was conducted using a 200 kV FEI Technai TEM equipped with a LaB6 source to analyse the size, shape, and elemental distribution of nanofibers.

The crystalline structure and phase of the membranes were examined using X-ray diffraction (XRD) with a Rigaku Smart Lab Diffractometer, scanning from 20˚ to 70˚ at a rate of 2˚/min with CuK radiation. Magnetic characteristics were assessed using a SQUID vibrating sample magnetometer (VSM) under a vibrating magnetic field of 4T at 300 K, recording zero-field-cooled (ZFC) and field-cooled (FC) states under a modest applied magnetic field of 100 Oe.

Raman measurements were conducted using a Horiba LABRAM high-resolution Raman spectrophotometer with a 633 nm He−Ne laser. Piezoresponse force microscopy, employing an atomic force microscopy (AFM) instrument equipped with a high-resolution scanning probe microscope (Bruker, Dimension ICON PT), was used to detect and characterize piezoelectric characteristics.

Fourier transform infrared spectroscopy (FTIR) was utilized to analyse functional groups using an Agilent Technologies (Model No. K8002AA Cary 660, USA) spectrophotometer with an ATR plate in the frequency range of 400 - 4000 cm^-1. UV-Vis spectroscopy (Shimadzu UV-2450) was employed to determine the concentration of dye after degradation. Atomic adsorption spectrometry (Analyst 400, PerkinElmer) was utilized to measure the adsorption quantity of heavy metals.

X-ray photoelectron spectroscopy (XPS) was used to analyse the surface chemical composition and oxidation states of MNFs NFs, detecting and validating the presence of heavy metals adsorbing to the surface. Thermogravimetric analysis (TGA) was carried out using a Perkin Elmer Thermal Analyzer equipment. Intermediate products of MB's photocatalytic, sono, and pyro-catalytic degradation were analysed using a Bruker HD compact mass spectrometer.

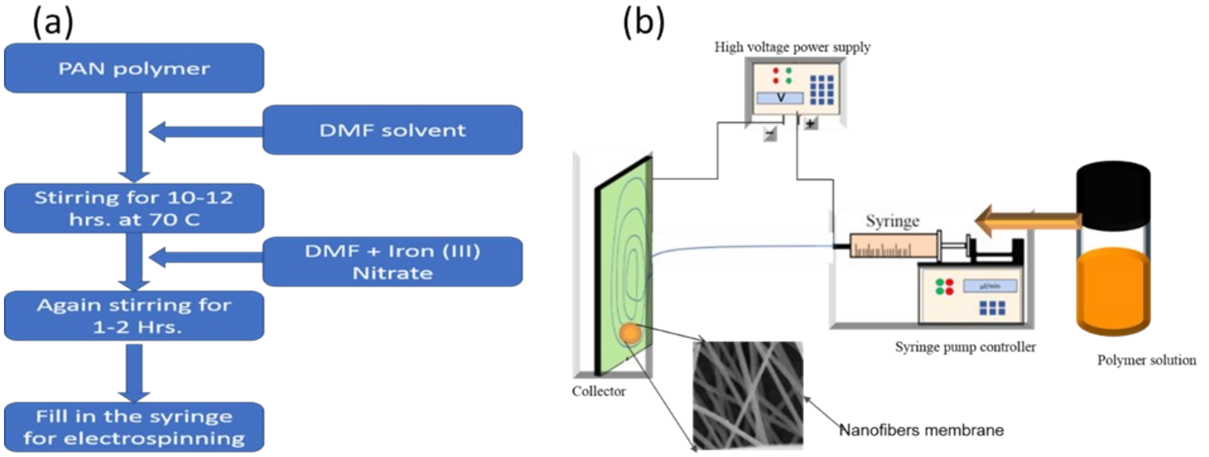

Figure S1. (a) Flow chart for solution preparation for nanofiber formation (b) Block diagram of electrospinning setup.

2. Synthesis parameter optimization of prepared MNFs

Controlled experiments were conducted to optimize the concentration of Iron (III) Nitrate. Figure 3 illustrates the optimization process, where SEM analysis of sample 2 revealed fine fibres within the range of 200 to 300 nm. Increasing the Iron (III) Nitrate concentration to 5% in sample 2 resulted in an increase in nanofiber diameter. Conversely, in sample 1, the use of 1% Iron (III) Nitrate concentration led to bead formation in the fibres.

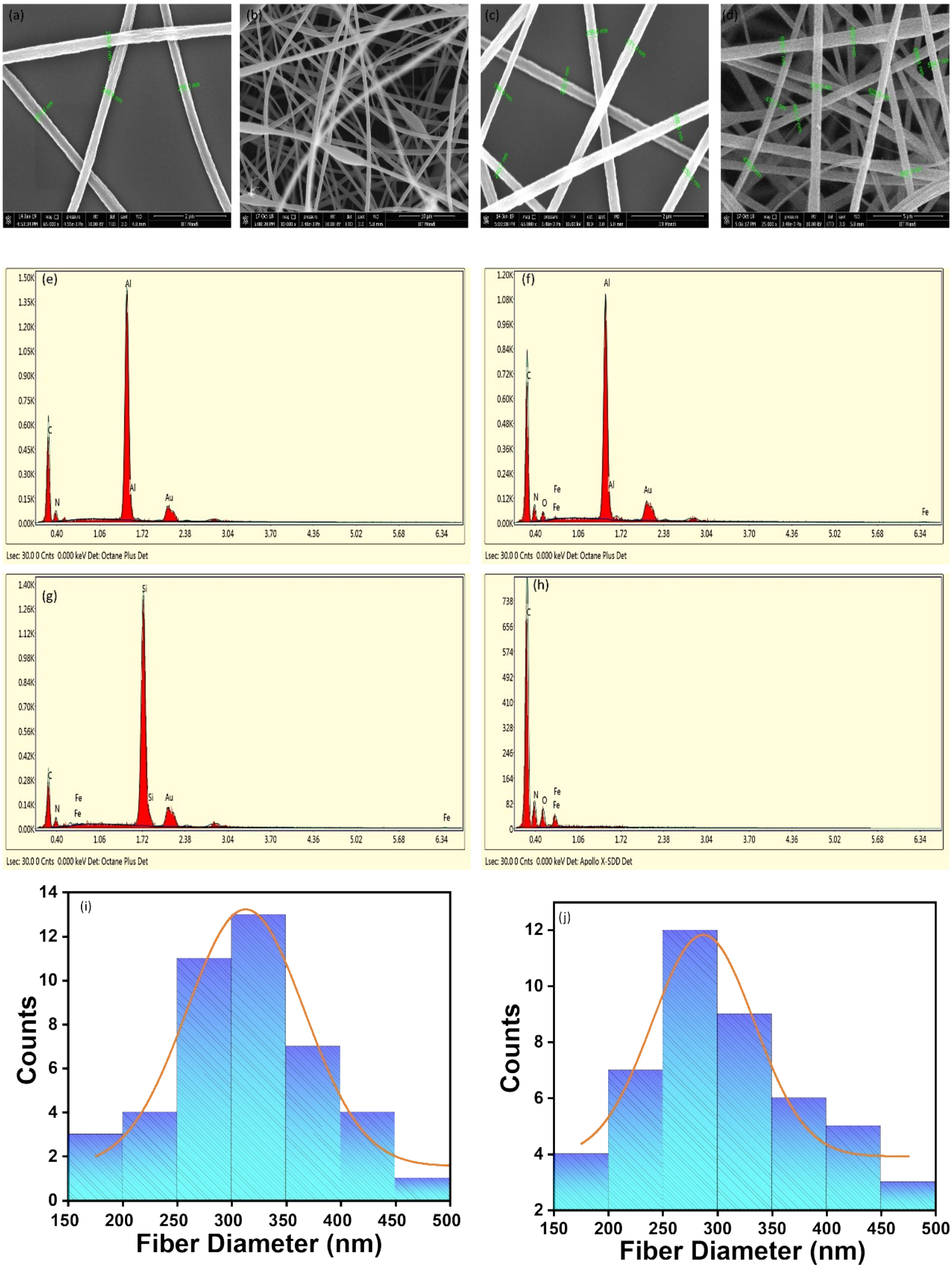

Figure S2: Scanning Electron Microscopy (SEM) images depicting (a) Polyacrylonitrile (PAN) NFs, (b) Sample 1, (c) Sample 2, (d) Sample 3. Elemental analysis displayed for (e) PAN nanofiber, (f) Sample 1, (g) Sample 2, (h) Sample 3. (i) Size distribution Histogram of the MNFs nanofibers (j) Size distribution Histogram of MNFs-C nanofibers

Table S1. Elemental analysis results of synthesized Magnetic Nanofibers (MNFs).

Elemental analysis (weight %)	PAN NFs	Sample 1	Sample 2	Sample 3
Carbon	60.0	58.5	57.4	56.2
Nitrogen	33.8	34.4	34.6	34.1
Oxygen	6.1	6.6	6.4	6.7
Iron	0.0	0.4	1.4	2.8

Error: for carbon c.a. 3.89%, oxygen c.a. 9%, nitrogen c.a. 7.8% and for iron c.a. 11.3% in EDAX analysis.

BET surface area and pore volume analysis were conducted on three different samples. The surface area and N2 adsorption-desorption were measured using the Brunauer-Emmett-Teller (BET) method. Typically, the surface area of electrospun nanofibers is reported to be less than 10m^2/g in existing literature. However, in this study, sample 2 exhibited a surface area of 21.0 m^2/g, nearly double the previous reports. As depicted in the figure, sample 2 displayed a higher surface area (21.0 m^2/g) compared to sample 1 (7.2 m^2/g) and sample 3 (10.5 m^2/g), indicating its superior potential for pollutant adsorption

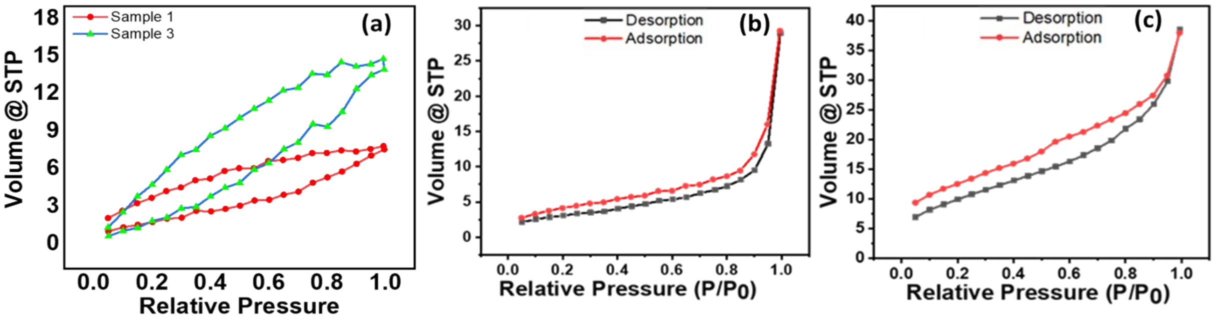

Figure S3. **BET surface area and pore volume analysis Illustration of adsorption and desorption isotherm along with pore size distribution of MNFs NFs**

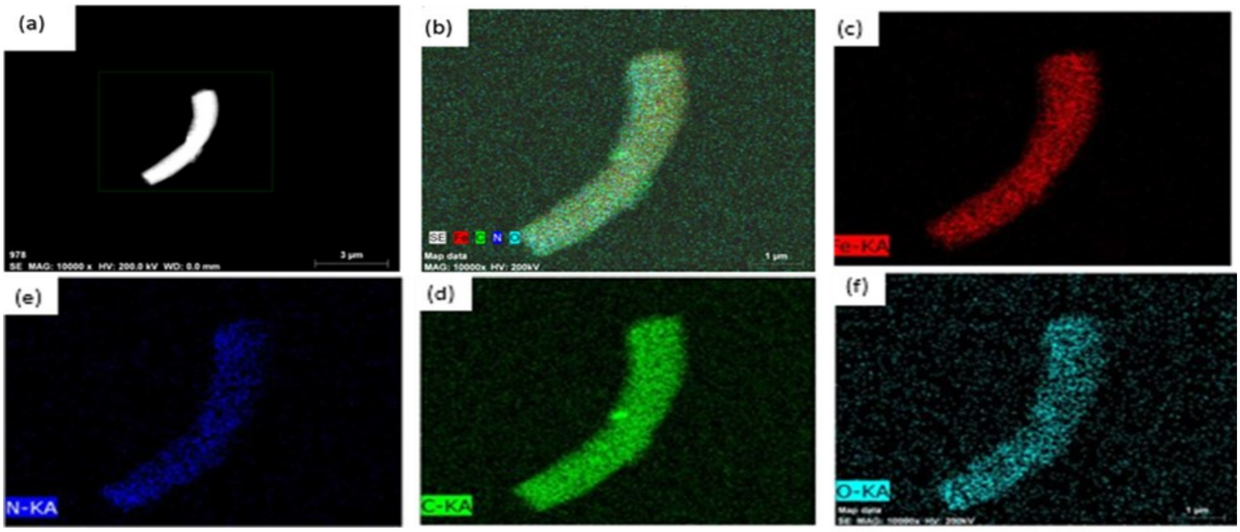

Figure S4 TEM images (a) TEM-HAADF image of MNF-C (Scale bar-3 µm). Elemental mapping of calcined MNFs NFs. (b) iron, (c) carbon, (d) overlay image, (e) nitrogen and (f) oxygen respectively. (Scale bar (b-f) – 1µm)

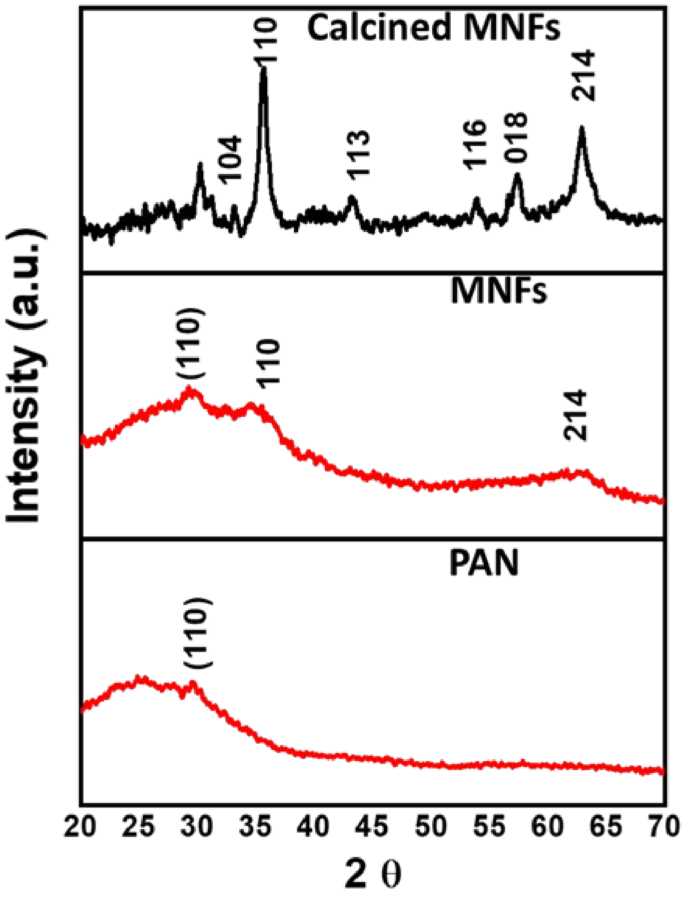

Figure S5. (a) X-Ray Diffraction (XRD) spectra comparison between (a) PAN NFs, (b) Electrospun α- Fe2O3/PAN NFs, (MNFs) and (c) Electrospun α- Fe2O3/PAN calcined MNF-C.

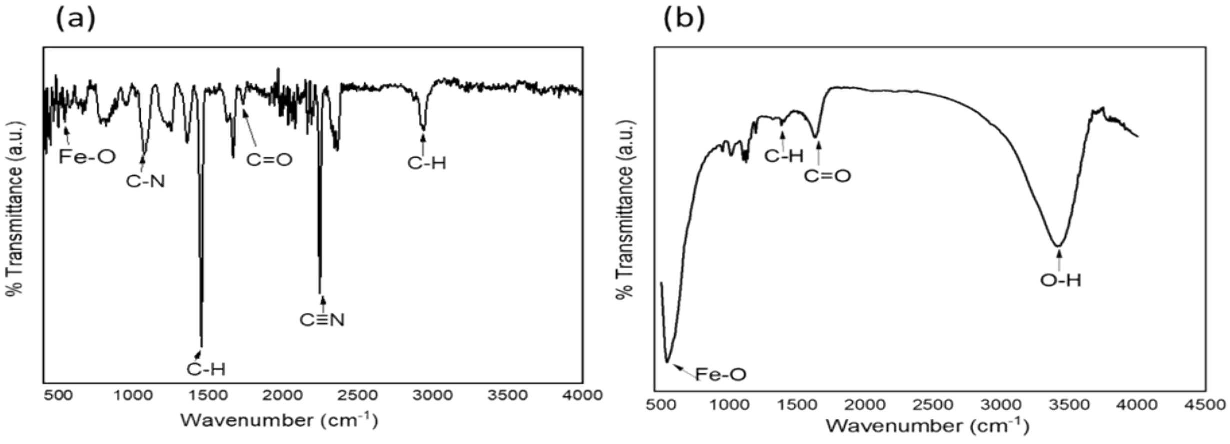

Figure S6 Fourier Transform Infrared Spectroscopy (FTIR) spectra of (a) MNFs and (b) MNFs-C.

Table S2 FTIR spectra analysis of MNFs and MNFs-C

Sample name	V(cm^{-1}) C-H	V(cm^{-1}) CN	V(cm^{-1}) C=O	V(cm^{-1}) Fe-O
MNFs	2930& 1452	2246	1739	
MNFs-C	1390	1068	1650	537

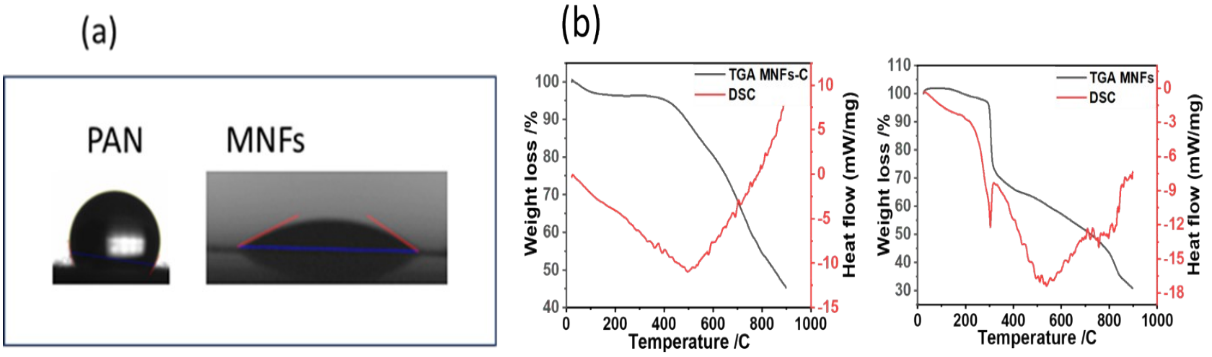

Figure S7. (a) (a) Contact angle measurement and (b) Thermogravimetric Analysis (TGA) and DSC analysis of (b) MNFs-C. and (b) MNFs mat.

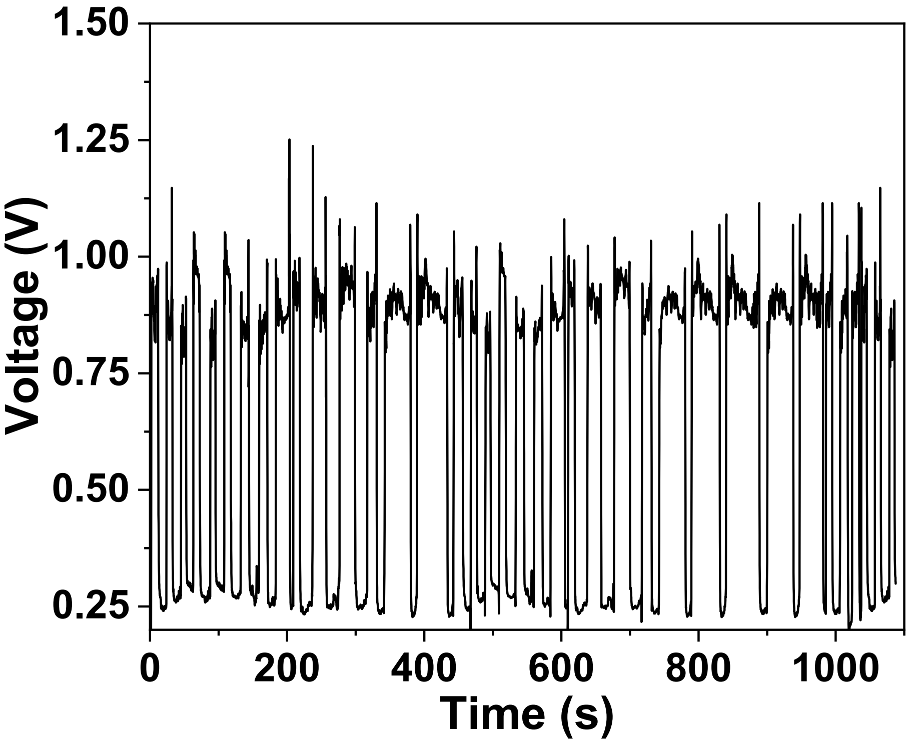

Figure S8 The voltage and current of the piezo device on the application of tapping force stability of the PENG device.

3. Mechanism of Photocatalysis degradation of MB

Doping and calcination of MNFs significantly enhance photocatalysis. The magnetic properties of the MNFs facilitate easy removal from the solution using a magnet. The schematic in Figure S8 of the SI illustrates the process of methylene blue degradation. Initially, the MNFs absorb visible light, generating electron-hole pairs. Electrons transition from the valence band (VB) to the conduction band (CB), while holes in the VB react with water or hydroxyl ions, generating hydroxyl radicals (OH*). Oxygen molecules present in the system lead to the formation of superoxide radicals (O2*), crucial for the degradation process. These active species (holes, O2* and OH*) oxidize the MB dye, ultimately converting it into harmless or even inert CO2 and H2O molecules.

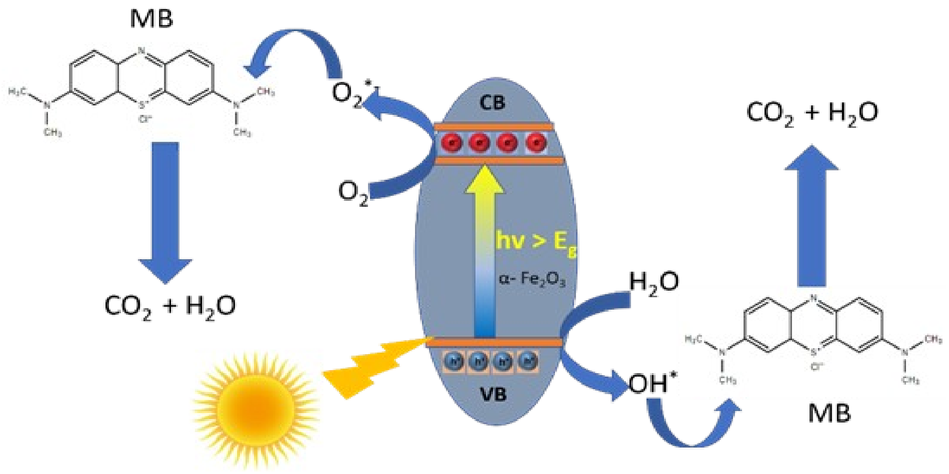

Figure S9. Schematic of photocatalytic degradation mechanism of MB

Table S3. A comprehensive representation of photocatalytic degradation of organic dyes as reported in literature.

Sr.No	**Catalyst**	**Pollutant**	**Pollutant (mg/L)**	**Visible light Catalyst (g/L)**	**Degradation efficiency (%)**	**Contact Time (min)**	**Ref**
1.	α-Fe_2O_3@rGO /PAN NCM	MB	20	-	98.5	30	[3]
2.	α-Fe_2O_3 /Graphene Composites + H_2O_2	RhB	10	-	98	20	[4]
3.	TiO2 + RGO	RhB	20	5	100	30	[5]
4.	Bi@CNT-α-Fe_2O_3 + H_2O_2	MB	20	0.06	100	20	[6]
5.	α-Fe_2O_3 fibre	CV	5	10	92	300	[7]
6.	MNFs	MB	20.7	0.4	98	240	This work

4. Mechanism of Sonocatalysis degradation of MB

Ultrasonic waves were employed to assess the piezocatalytic properties of the materials. Samples were electrodeposited with silver paste and immersed in deionized water to examine the impact of ultrasonic waves on piezoelectric activity. Our investigation revealed that ultrasonic waves enabled us to monitor AC output voltages using an oscilloscope. Data were collected periodically under both ultrasonication on and off conditions, as depicted in the accompanying figure. These results confirm the piezoelectric activity of the α-Fe2O3/PAN sample.

The catalytic reaction process involves four steps: energy absorption, conversion, transfer, and surface reaction in the heterojunction structure. Reactant molecules adsorb onto the surface of the heterojunction in the calcined MNFs structure, forming smaller, more efficiently sorbing organic pollutants. Sonication positively influences both oxidation and reduction reactions of the targeted pollutant. Digital storage oscilloscope (DSO) analysis of voltage versus time measurements for pristine PAN mat and calcined MNFs matis shown in Figure 5(e). The results indicate that the calcined mat exhibits a voltage of approximately 0.5 volts, which surpasses the pristine PAN mat's 0.2 volts under the same conditions.

Sr No	Catalyst	Pollutant	Pollutant (mg/L)	Ultrasonic Catalyst (g/L)	Degradation efficiency (%)	Contact Time (min)	Ref
1	CuZnTi-LDHs	MB	5	0.75	87	90	[8]

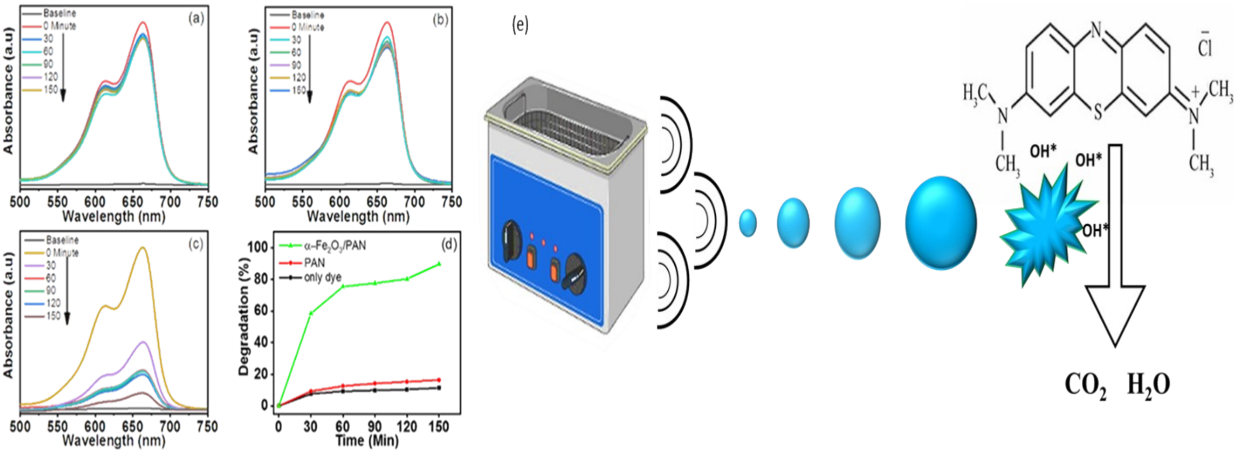

Figure S10. Sonocatalytic performance of (a) With MB without any catalyst (b) with PAN nanofiber (c) with MNFs With nano fiber (d) The degradation percentage

Table S4. Comparison Table of Sonocatalysis of Various Organic Dyes in the Literature

.

2	$CaMoO_4^{-7}$	Acid Orange 7	5	1	97	120	[9]
3	$CoFe_2O_4$-rGO	Acid Orange 7	10	0.08	90.5	120	[10]
4	Fe–C_{60}/TiO_2	MB	3.19	1	95	150	[11]
5	TiO_2-CNT anatase	MB	3.19	1	100	120	[12]
6	ZnSe-GR/TiO_2	RhB	9.5	2	82	150	[13]
7	ZnO/GR/TiO_2	MB	20	1	79	120	[14]
8	TiO_2- CNT	MB	10	0.25	90	120	[15]
9	$CoFe_2O_4$@ZnS + H_2O_2	MB	25	0.5	100	70	[16]
1	GQDs anchored CdSe	MB	20	1	99	90	[17]
1	CuS/CFO	MB	25	0.5	100	30	[18]
1	CuS/CFO	RhB	25	0.5	72	30	
1	MNFs	MB	20.7	0.4	94	150	This work

5. Mechanism of Pyrocatalysis degradation of MB

Pyrocatalysis originates from the intrinsic polarization of pyroelectric materials, where the dipole moment (Ps) is inherently nonzero. This results in bonded polarized charges on opposite sides of the material's inner surface. Under stable temperatures, these polarized charges are offset by absorbed charges of equal magnitude but opposite polarity, rendering the material electrically neutral. Upon heating, the density of Ps decreases due to dipole moment disorientation, leading to charge compensation and the generation of O2*- radicals. Conversely, a negative temperature gradient increases Ps density, causing dipole moment reorientation, charge adsorption, and OH* radical formation on the surface. The breakdown of dye solutions occurs through a sequence of chain reactions involving highly reactive oxidative species, namely O2*- and OH* radicals. Chemical equations elucidate the pyro electrochemical degradation of dyes through mechanistic analysis. It's worth noting that pyroelectric materials possess a polar character, making them piezoelectric, although not all piezoelectric materials exhibit pyroelectricity.

$$MFNsC \rightarrow^{\Delta t} MFNs + e^{-} + h^{+}$$

$$O_2 + e^{-} \rightarrow O_2{}^{*-}$$

$$OH^{-} + h^{+} \rightarrow OH^{*}$$

$$OH^{*} \ or \ O_2{}^{*-} + MB \rightarrow (degradation)$$

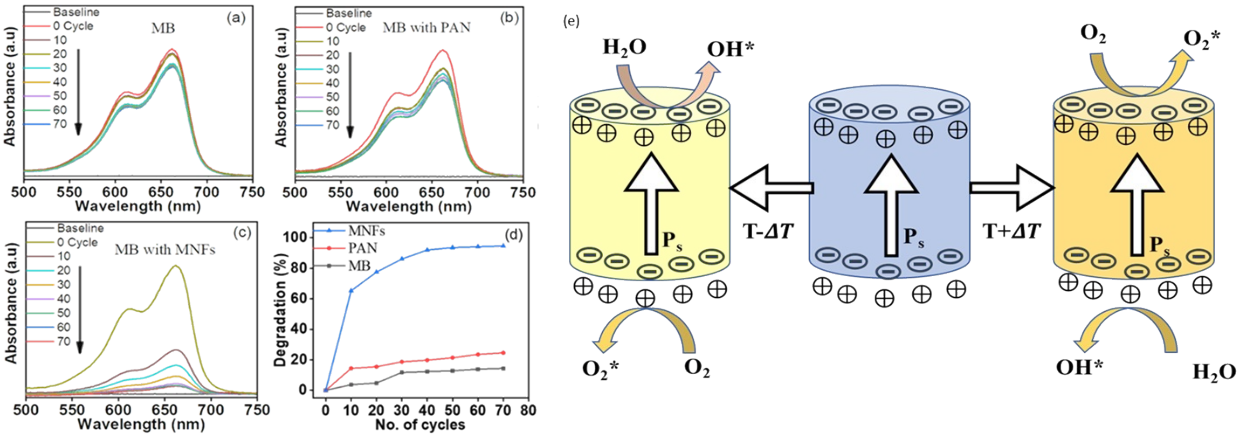

Figure S11. Pyro catalytic performance of (a) With MB without any catalyst (b) With PAN nanofiber (c) With MNFs nanofiber (d) The Degradation percentage.

T**able S5. comparative study of Pyro catalytic activity of MNFs with some reported catalyst in the degradation of various dyes.**

No	Catalyst	Type of sample	Dye	Dye (mg/L)	Temperature limit (°C)	No of hot-cold sets	Degradation (%)	Ref
1	$BaTiO_3$ @ Ag	Nanofibers	RhB	5	30-52	72	92	[19]
2	$BaTiO_3$ @ Pd	Nanofibers	RhB	5	30-52	72	95	
3	$BiFeO_3$	Nanoparticles	RhB	5	27-38	85	99	[20]
4	Black phosphorene	nanosheets	RhB	5	15-65	100	5	[19]
5	PAN	Nanofibers	MB	20.7	10-40	70	22	This work
6	MNFs	Nanofibers	MB	20.7	10-40	70	94	This work

6 Identification of intermediate products of MB degradation

The degradation of methylene blue (MB) was accomplished through the interpretation of fragment ions in the mass spectra and comparison with commercial standards. The intermediates, along with their corresponding molecular weights, are presented in Figure S10 of the supplementary information.

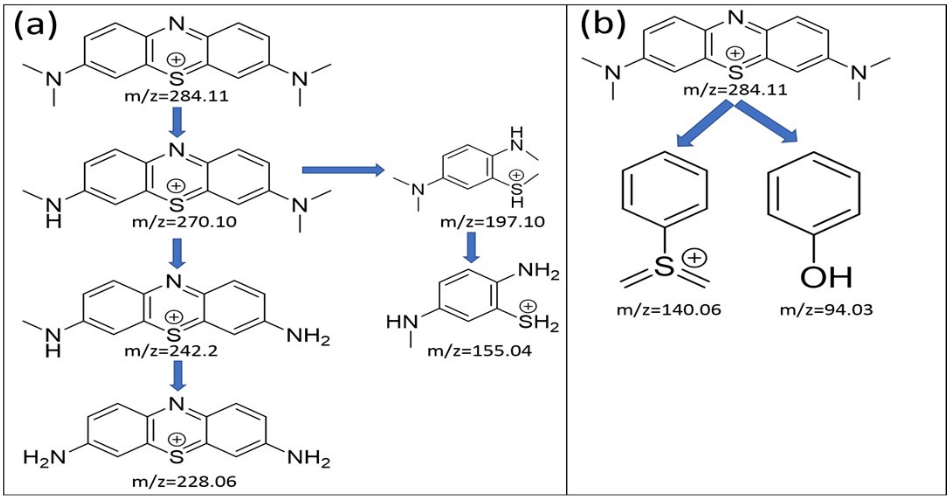

Figure S12. The intermediate species formed in the process of photocatalytic degradation studies which followed two pathways. (a) Sequential degradation of MB and (b) Immediate degradation of MB respectively.

Mass spectroscopy analysis

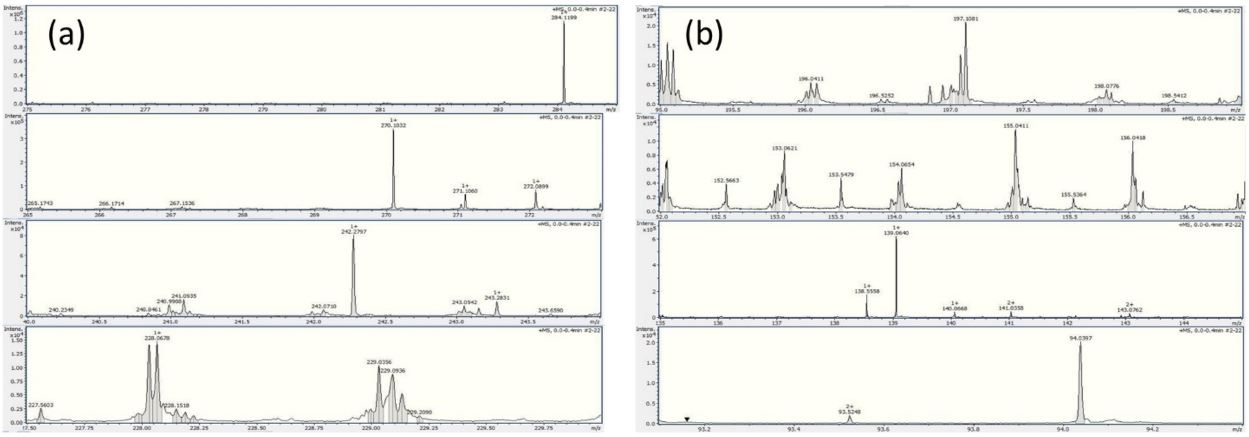

Figure S13. Mass spectroscopy analysis of the intermediates of the MB (a) initial breakdown (b) smaller mass molecules

7. Methylene blue (MB) adsorption studies

Methylene blue (MB) adsorption onto MNFs NFss for potential water filtration was investigated. Solutions with various MB concentrations (10-250 ppm) were filtered through the membrane, and decolorization was assessed using UV-Vis spectroscopy. Figure S12(a) illustrates complete decolorization of lower concentration MB solutions after filtration with MNFs NFss. Removal efficacy was approximately 95% for higher concentrations, as shown in the inset of Figure S12(b). However, for lower concentrations, the removal efficiency reached around 99%. Figure S13 depicts the adsorption and desorption processes. MNFs NFss exhibited high removal efficiency of MB, enabling layer-by-layer stacking to enhance water filter membrane performance, particularly for industrial applications dealing with organic pollutants at high concentrations.

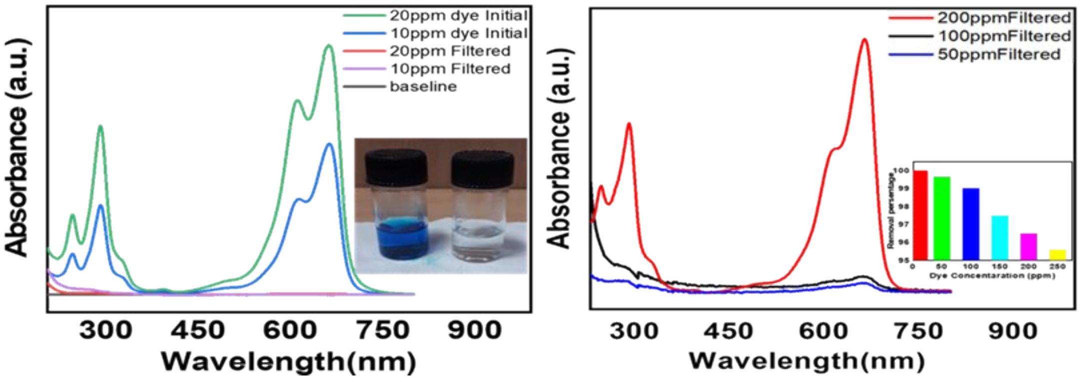

Figure S14. (a) MB filtration using MNFs mat at 10 ppm and 20 ppm concentrations. (b) MB filtration using MNFs mat for higher concentrations (10-200 ppm). (Inset Figure 3b- MB percentage removal efficiency at various concentration (10-200 ppm).

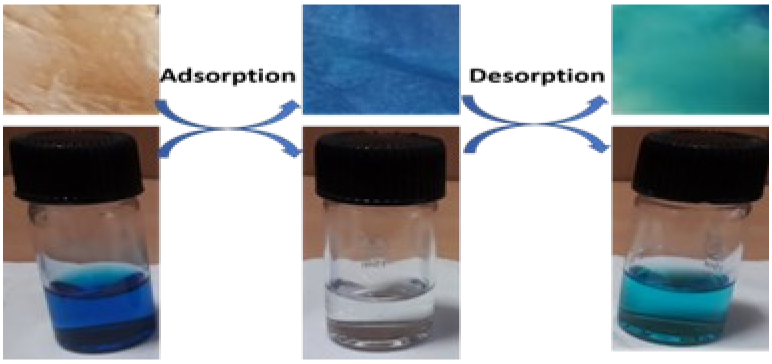

Figure S15. Adsorption and desorption of MB dye.

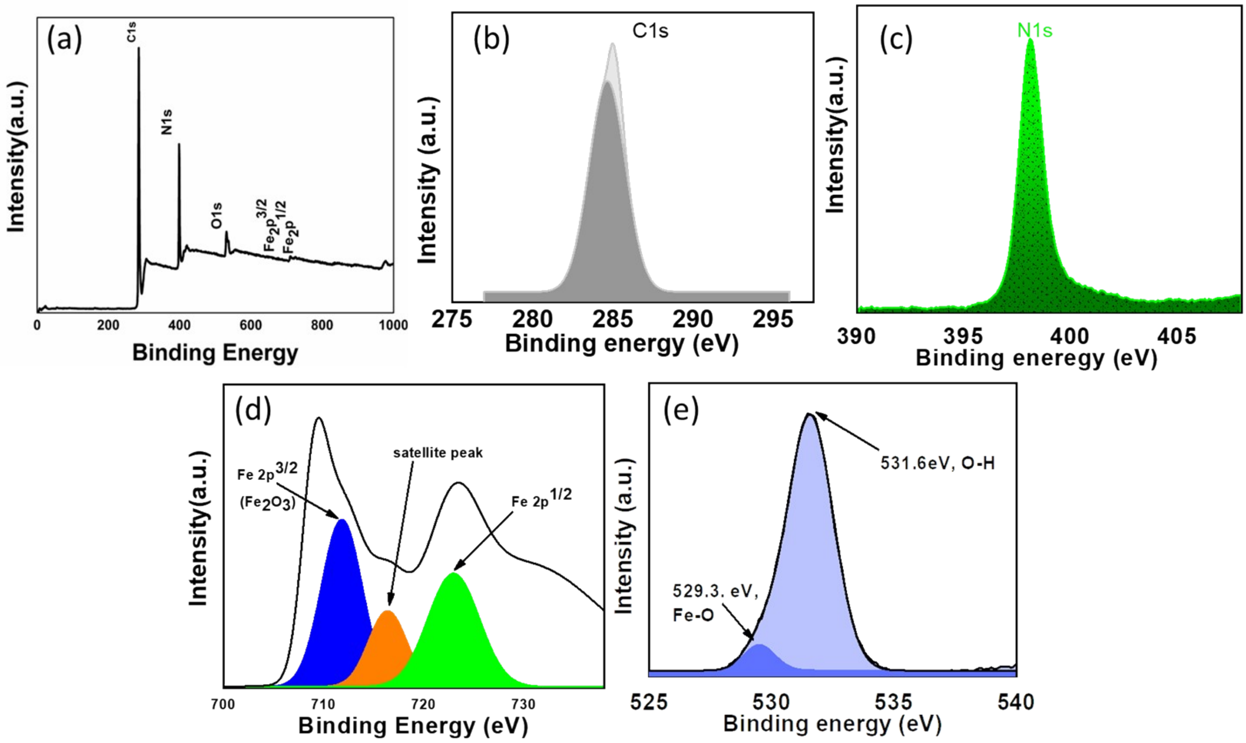

Figure S16. XPS spectra of the MNFs NFs. (a) Full survey XPS spectrum (b) High resolution C1s spectra (c) High resolution N1s spectra (d) Deconvoluted high Fe2p spectra and (e) High resolution O1s spectra respectively.

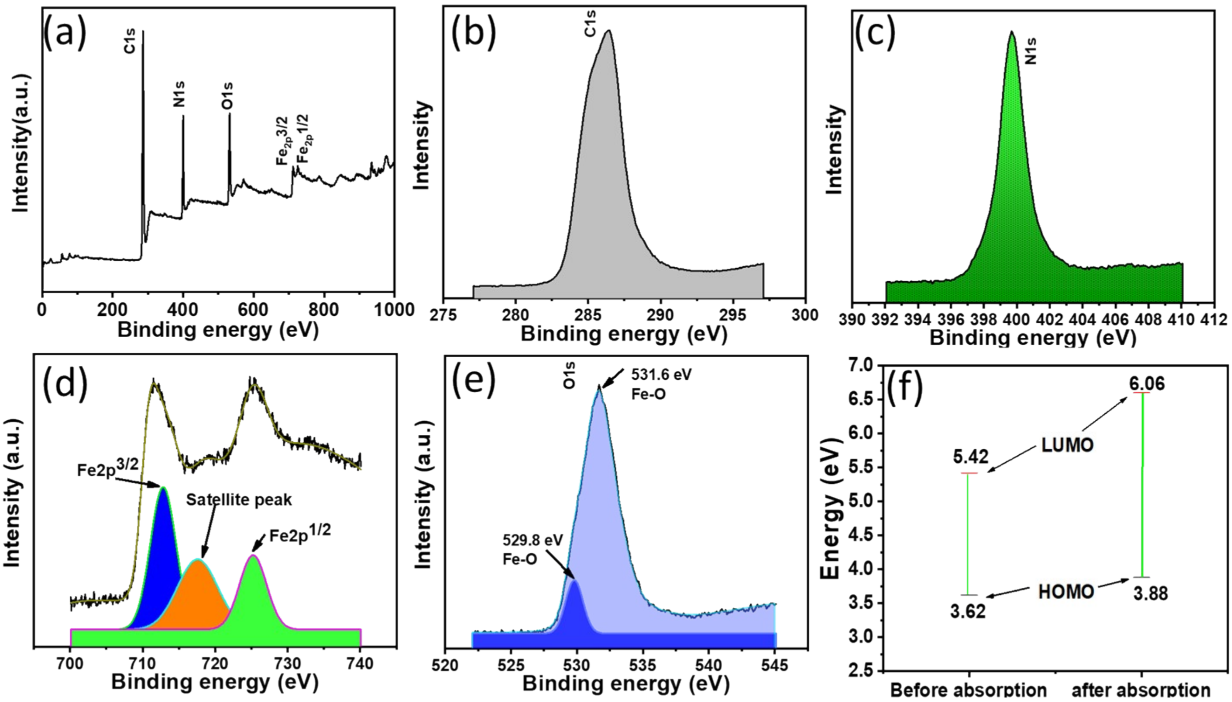

Figure S17. XPS spectra of the MNFs NFs after MB absorption. (a) Full survey XPS spectrum (b) High resolution C1s spectra (c) High resolution N1s spectra (d) Deconvoluted high Fe2p spectra and (e) High resolution O1s spectra and (f) HOMO LUMO energy band gap for MNFs nanofibers respectively.

8. Heavy metals detection

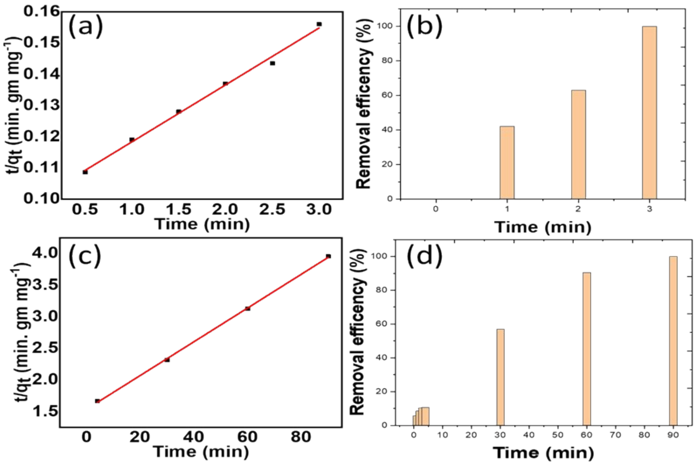

Figure S18. (a) Lead adsorption pseudo second order kinetic model, (b) removal efficiency of lead, (c) copper adsorption pseudo second order kinetic model, and (d) removal efficiency of copper respectively.

Elemental analysis (percentage) of metals detected from XPS spectra To investigate the adsorption mechanism of heavy metals on the MNFs mat, we examined the surface chemical composition changes before and after heavy metal adsorption using XPS. The presence of Pb and Cu species after adsorption indicates that Pb^{2+} and Cu^{2+} were adsorbed on the surface of the MNFs.

Table S6. Elemental study comparison of MNFs mat before and after heavy metals adsorption.

Before adsorption		After adsorption
Metals	Atomic %	Atomic %
C1s	68.3	70.2
N1s	16.9	15.4

O1s	14.2	13.6
Fe2p	0.5	0.3
Pb4f		0.08
Cu2p		0.1

The Fe2+/Fe3+ ratios decreased with the improvement of calcination temperature, revealing that part of Fe2+ cations were translated to Fe3+ during the calcination process. And the Fe3+ cations play a key role in the formation of O2− species, which could effectively degrade

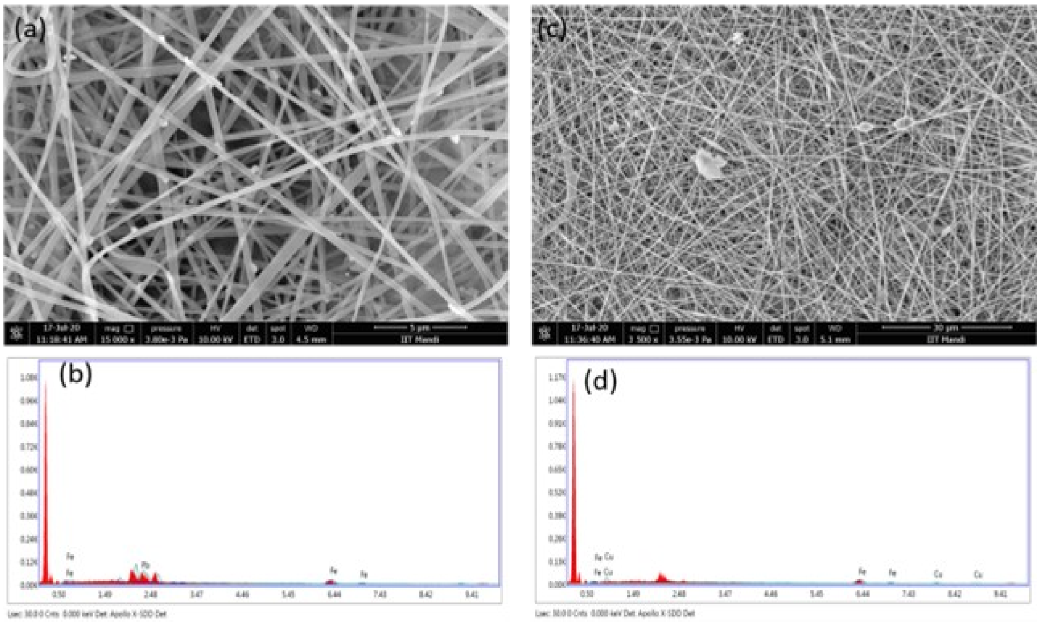

Figure S19. SEM images and EDAX analysis of MNFs mat after heavy metal filtration. (a, b) SEM and EDAX spectra after Pb filter, (c, d) SEM and EDAX spectra after Cu filter.

References

[1] R. K. Sadasivam, S. Mohiyuddin, and G. Packirisamy, “Electrospun polyacrylonitrile (PAN) Templated 2D Nanofibrous Mats: A platform toward practical applications for dye removal and bacterial disinfection,” *ACS Omega*, vol. 2, no. 10, pp. 6556–6569, 2017.

[2] S. S. Syed Bakar, K. M. Foong, N. Abdul Halif, and S. Yahud, “Effect of solution concentration and applied voltage on electrospun polyacrylonitrile fibers,” in *IOP Conference Series: Materials Science and Engineering*, 2019, vol. 701, no. 1, pp. 1–8.

[3] K. Sun, L. Wang, C. Wu, J. Deng, and K. Pan, “Fabrication of α-Fe2O3@rGO/PAN Nanofiber Composite Membrane for Photocatalytic Degradation of Organic Dyes,” *Adv. Mater. Interfaces*, vol. 4, no. 24, pp. 1–7, 2017.

[4] “One-Step Hydrothermal Synthesis of 2D Hexagonal Nanoplates of α-Fe2O3_Graphene Composites with Enhanced Photocatalytic Activity.pdf.” .

[5] D. Liang *et al.*, “One-step hydrothermal synthesis of anatase TiO2/reduced graphene oxide nanocomposites with enhanced photocatalytic activity,” *J. Alloys Compd.*, vol. 582, pp. 236–240, Jan. 2014.

[6] A. A. Manda *et al.*, “Enhanced photocatalytic degradation of methylene blue by nanocomposites prepared by laser ablation of Bi on CNT-α-Fe2O3 nanoparticles,” *Optics and Laser Technology*, vol. 155. 2022.

[7] R. N. Araujo *et al.*, “α-Fe2O3 fibers: An efficient photocatalyst for dye degradation under visible light,” *Journal of Alloys and Compounds*, vol. 882. 2021.

[8] H. Daneshvar, M. S. Seyed Dorraji, A. R. Amani-Ghadim, and M. H. Rasoulifard, “Enhanced sonocatalytic performance of ZnTi nano-layered double hydroxide by substitution of Cu (II) cations,” *Ultrason. Sonochem.*, vol. 58, no. April, p. 104632, 2019.

[9] L. L. He *et al.*, “Synthesis of CaMoO4 microspheres with enhanced sonocatalytic performance for the removal of Acid Orange 7 in the aqueous environment,” *Sep. Purif. Technol.*, vol. 276, no. June, 2021.

[10] A. Hassani, G. Çelikdağ, P. Eghbali, M. Sevim, S. Karaca, and Ö. Metin, “Heterogeneous sono-Fenton-like process using magnetic cobalt ferrite-reduced graphene oxide (CoFe2O4-rGO) nanocomposite for the removal of organic dyes from aqueous solution,” *Ultrasonics Sonochemistry*, vol. 40. pp. 841–852, 2018.

[11] Z. Da Meng and W. C. Oh, “Sonocatalytic degradation and catalytic activities for MB

solution of Fe treated fullerene/TiO2 composite with different ultrasonic intensity," *Ultrasonics Sonochemistry*, vol. 18, no. 3. pp. 757–764, 2011.

[12] K. Zhang, F. J. Zhang, M. L. Chen, and W. C. Oh, "Comparison of catalytic activities for photocatalytic and sonocatalytic degradation of methylene blue in present of anatase TiO2-CNT catalysts," *Ultrasonics Sonochemistry*, vol. 18, no. 3. pp. 765–772, 2011.

[13] L. Zhu, S.-B. Jo, S. Ye, K. Ullah, and W.-C. Oh, "Rhodamine B degradation and reactive oxygen species generation by a ZnSe-graphene/TiO2 sonocatalyst," *Chinese J. Catal.*, vol. 35, no. 11, pp. 1825–1832, Nov. 2014.

[14] P. Nuengmatcha, S. Chanthai, R. Mahachai, and W. C. Oh, "Sonocatalytic performance of ZnO/graphene/TiO2 nanocomposite for degradation of dye pollutants (methylene blue, texbrite BAC-L, texbrite BBU-L and texbrite NFW-L) under ultrasonic irradiation," *Dye. Pigment.*, vol. 134, pp. 487–497, Nov. 2016.

[15] E. Alves Nunes Simonetti, L. D. S. Cividanes, T. M. Bastos Campos, F. Williams Fernandes, J. P. B. MacHado, and G. P. Thim, "Sonocatalytic degradation of methylene blue in the presence of TiO2 doped carbon nanostructures-catalytic and adsorption comparison by different carbon forms," *Fullerenes Nanotub. Carbon Nanostructures*, vol. 23, no. 8, pp. 725–733, 2015.

[16] S. Farhadi, F. Siadatnasab, and A. Khataee, "Ultrasound-assisted degradation of organic dyes over magnetic CoFe2O4@ZnS core-shell nanocomposite," *Ultrason. Sonochem.*, vol. 37, pp. 298–309, 2017.

[17] S. Sajjadi, A. Khataee, and M. Kamali, "Sonocatalytic degradation of methylene blue by a novel graphene quantum dots anchored CdSe nanocatalyst," *Ultrasonics Sonochemistry*, vol. 39. pp. 676–685, 2017.

[18] F. Siadatnasab, S. Farhadi, and A. Khataee, "Sonocatalytic performance of magnetically separable CuS/CoFe2O4 nanohybrid for efficient degradation of organic dyes," *Ultrason. Sonochem.*, vol. 44, pp. 359–367, Jun. 2018.

[19] J. Ma *et al.*, "High pyrocatalytic properties of pyroelectric BaTiO3 nanofibers loaded by noble metal under room-temperature thermal cycling," *Ceram. Int.*, vol. 44, no. 17,

pp. 21835–21841, 2018.

[20] J. Wu *et al.*, “Strong pyro-catalysis of pyroelectric BiFeO3 nanoparticles under a room-temperature cold-hot alternation,” *Nanoscale*, vol. 8, no. 13, pp. 7343–7350, 2016.